Exploring the test of the no-hair theorem with LISA

Chantal Pitte,[1,*] Quentin Baghi,[2,1] Marc Besançon,[1] and Antoine Petiteau[1,2]

[1]*IRFU, CEA, Université Paris-Saclay, F-91191, Gif-sur-Yvette, France.*
[2]*Astroparticule et Cosmologie, Université de Paris, CNRS, Paris, 75013, France*

(Dated: June 21, 2024)

In this study, we explore the possibility of testing the no-hair theorem with gravitational waves from massive black hole binaries in the frequency band of the Laser Interferometer Space Antenna (LISA). Based on its sensitivity, we consider LISA's ability to detect possible deviations from general relativity (GR) in the ringdown. Two approaches are considered: an agnostic quasi-normal mode (QNM) analysis, and a method explicitly targeting the deviations from GR for given QNMs. Both approaches allow us to find fractional deviations from general relativity as estimated parameters or by comparing the mass and spin estimated from different QNMs. However, depending on whether we rely on the prior knowledge of the source parameters from a pre-merger or inspiral-merger-ringdown (IMR) analysis, the estimated deviations may vary. Under some assumptions, the second approach targeting fractional deviations from GR allows us to recover the injected values with high accuracy and precision. We obtain $(5\%, 10\%)$ uncertainty on $(\delta\omega, \delta\tau)$ for the $(3,3,0)$ mode, and $(3\%, 17\%)$ for the $(4,4,0)$ mode. As each approach constrains different features, we conclude that combining both methods would be necessary to perform a better test. In this analysis, we also forecast the precision of the estimated deviation parameters for sources throughout the mass and distance ranges observable by LISA.

I. INTRODUCTION

The first detection of gravitational waves (GWs) with LIGO [1, 2] produced by the coalescence of the black hole binary (BHB) GW150914 [3], marked the beginning of the GW astronomy era. At the same time, its detection opened a window to probe physics beyond the standard model and general relativity (GR). Since that first detection, the scientific community has been eager to test GR in the strong field regime [4–7].

One of the most considered tests nowadays is the test of the no-hair theorem [8, 9] in the ringdown of BHB. In the last stage of the coalescence, once formed, the perturbed BH will settle down through the emission of GWs. In perturbation theory (PT), the radiation of a Kerr BH can be written as a superposition of damping sinusoidals [10–15]. The strain in the plus and cross polarizations reads

$$h_+(t) - ih_\times(t) = \sum_{lmn} h_{lmn}(t)\,{}_{-2}S_{lmn}(a_f\tilde{\omega}_{lmn};\theta,\varphi), \quad (1)$$

where

$$h_{lmn}(t) = A_{lmn}e^{i(\phi_{lmn} - \tilde{\omega}_{lmn}t)}. \quad (2)$$

The equations describing a perturbed Kerr BH were first derived in [10]. A companion paper describes the subsequent radiation of gravitational waves [11] and introduces solutions in terms of spin-weighted spheroidal harmonics ${}_sS_{lmn}(a_f\tilde{\omega}_{lmn};\theta,\varphi)$ with $s = -2$ denoting the spin of the field. They depend on the phase φ and on the angle θ between the normal of the orbital plane and the observer. Each harmonic is labeled by (l, m, n) as polar and azimuthal angular numbers, and overtone respectively. Their eigenvalues are complex frequencies known as quasi-normal modes (QNMs) [13, 14]. Where the real part is the oscillation frequency, while the imaginary part corresponds to the damping time

$$\tilde{\omega}_{lmn} = \omega_{lmn} + i/\tau_{lmn}. \quad (3)$$

The metric structure characterizes the QNMs' values; thus, for a remnant Kerr BH, they depend only on the mass and spin (M_f, a_f) [8, 10]. In contrast, the amplitude and phase associated with each mode (A_{lmn}, ϕ_{lmn}) correspond to their excitation in the pre-merger phase, thus depending on the initial black holes' parameters [16, 17].

One approach to probe the no-hair conjecture is to use *BH spectroscopy* [13–15, 18, 19]. In GR, the values of the BH spectrum are defined solely by the mass and spin of the final BH. Therefore, when studying the spectrum of the remnant BH, one can trace back to those parameters [20–23]. Then, the comparison of pairs of mass and spin obtained from different QNMs should be consistent with each other. In an alternative theory to GR, the values of the complex frequencies might deviate from those of GR [9, 24, 25]. Thus, the pairs of mass and spin derived from each QNM would not be consistent [16, 26]. Note that more than one QNM is required to perform this analysis. There exists another method where only one QNM is needed: it involves the comparison of estimated parameters in the pre-merger and post-merger phases.

To this day, while the fourth observational run (O4) is ongoing, over a hundred sources have been detected by the LIGO-Virgo-Kagra (LVK) Collaboration [27, 28].

* chantal.pitte@cea.fr

Nevertheless, the signature of QNMs seems to hide below the noise floor. Hints of spherical higher harmonics have been found [29] in the full inspiral-merger-ringdown (IMR) waveform for some events. Furthermore, the presence of the first overtone of the dominant QNM, i.e. (2, 2, 1), has been inferred for the first event GW150914 [30, 31] (see the discussion on its detectability [32–35]). As the sensitivity of current and future interferometers increases [2, 36, 37], we expect to detect more QNMs, hopefully already from the O4 analysis. However, the question of whether we can unmistakably observe a deviation from GR remains. Up to the O3 catalog, various analyses have been made with results always in agreement with GR [4–7, 38, 39]. More reliable analyses to confidently discriminate any alternative theory would rely on a null hypothesis comparison in a Bayesian approach. However, this endeavor presents quite a challenge, since it would require that BH's spectra be solved for alternative theories. Various developments in computing beyond-GR BH's spectra have been undertaken, primarily for static or slowly rotating BHs in different alternative theories, e.g. [24, 25, 40, 41], see nonetheless [42] for rapidly rotating BHs in effective field theories. In the lack of waveform catalogs including deviations from GR, the best we can do is to allow for deviations of GR in a model-independent way, in the injection and search templates.

As the Laser Interferometer Space Antenna (LISA) passed the adoption phase, the moment to detect massive black hole binary (MBHB) mergers with high signal-to-noise ratio (SNR) approaches [37, 43]. With high SNR, high precision is also expected. Therefore, in sources where the detectability of higher harmonics is possible [44], we also expect to detect various QNMs.

In this exploratory study, we address the question of the extent to which LISA becomes distinctively sensitive to a deviation from GR in the ringdown phase of BHB coalescence. In a similar context, possible deviations from GR with LISA sources have been studied in [45] using the pSEOBNRv5HM waveform [39, 46]. In that work, the full IMR was used to find deviations present only in the ringdown. While using the full IMR is an advantage for low SNR sources, for high SNR, systematic errors in the full IMR waveform might bias the estimated parameters of the remnant if eccentricity, precession, or higher harmonics are not accounted for. In this work, we consider a more flexible prior knowledge of parameters, assuming a raw posterior distribution of the final BH parameters estimated from the IMR as uniform priors for this analysis. We use two approaches to assess LISA sensitivity to detect deviations from GR. We will also discuss the outcome of different assumptions on the priors.

The paper is divided as follows. In Sec. II, we describe the response of LISA to gravitational waves. Sec. III is dedicated to the methodology implemented, including a description of the data, the templates, and the likelihood computation. In Sec. IV we show and comment on the results. We then forecast how the GR test precision relates to SNR in Sec. V. We conclude in Sec. VI.

II. LISA RESPONSE TO WAVEFORMS

LISA consists of three spacecrafts (S/C) in heliocentric orbits and arranged in a triangular formation with arms of 2.5×10^6 km. One reason for this particular setup is that with different combinations of individual phasemeter measurements, one can construct multiple synthetic interferometers.

GWs crossing the beam paths will imprint a frequency shift between the emitted and received light at the detectors. The measurement at the end of each arm is called the [illegible] is defined as

$$y_{rs}(t_r) \simeq \frac{1}{2\left(1-\mathbf{k}\cdot\hat{\mathbf{n}}_{rs}(t_r)\right)}\left[H_{rs}\left(t_r - L_{rs}(t_r) - \mathbf{k}\cdot\mathbf{x}_r(t_r)\right) - H_{rs}\left(t_r - \mathbf{k}\cdot\mathbf{x}_s(t_r)\right)\right]. \tag{4}$$

We use geometric units $c = G = 1$ throughout the whole study. Lower indices r and s take values from 1 to 3 for the three S/C, representing the light-receiving and the light-sending spacecraft respectively. The S/C positions are defined by $\mathbf{x}_{r,s}$. L_{rs} is the arm's length between the two S/C. The vector $\mathbf{k}$ defines the direction of propagation of the GW, while $\hat{\mathbf{n}}_{rs}$ denotes the direction of the beam. Lastly, H_{rs} is the source's gravitational strain pro[illegible]

$$\begin{aligned} H_{rs}(t) = {} & \left(h_+(t)\cos 2\psi - h_\times(t)\sin 2\psi\right)\hat{\mathbf{n}}_{rs}(t)\cdot\mathbf{e}_+\cdot\hat{\mathbf{n}}_{rs}(t) \\ & + \left(h_+(t)\sin 2\psi + h_\times(t)\cos 2\psi\right)\hat{\mathbf{n}}_{rs}(t)\cdot\mathbf{e}_\times\cdot\hat{\mathbf{n}}_{rs}(t), \end{aligned} \tag{5}$$

where $\mathbf{e}_{+,\times}$ are the polarization tensors defined in the traceless-tra[illegible]

[illegible] (6)

as

$$\mathbf{e}_+ = \mathbf{u}\otimes\mathbf{u} - \mathbf{v}\otimes\mathbf{v}, \tag{7a}$$

$$\mathbf{e}_\times = \mathbf{u}\otimes\mathbf{v} + \mathbf{v}\otimes\mathbf{u}. \tag{7b}$$

Vectors $\mathbf{v}$ and $\mathbf{u}$ together with the propagation vector $\mathbf{k}$ in spherical coordinates locate the source in the observation [illegible]

$$\mathbf{u} = \{\sin\lambda, \cos\lambda, 0\}, \tag{8a}$$

$$\mathbf{v} = \{-\sin\beta\cos\lambda, -\sin\beta\sin\lambda, \cos\beta\}, \tag{8b}$$

$$\mathbf{k} = \{-\cos\beta\cos\lambda, -\cos\beta\sin\lambda, -\sin\beta\}, \tag{8c}$$

with β, λ the ecliptic latitude and longitude respectively.

LISA does not work like a regular Michelson interferometer, as its interferometry is synthetically performed on the ground in the post-processing. Given that LISA arms will not have an equal length in space, nor would they be stationary, particular linear combinations with time delays of links are needed to cancel the noise produced from fluctuations in the laser [47–52] among others noises. Those combinations are known as time delay interferometry (TDI) channels (X, Y, Z), and will be used in the following,

$$X = (1 - D_{121} - D_{12131} + D_{1312121})(y_{13} + D_{13}y_{31}) - (1 - D_{131} - D_{13121} + D_{1213131})(y_{12} + D_{12}y_{21}) , \tag{9}$$

where D_{ij} is the delay operator [53],

$$D_{rs}\, f(t) = f\,(t - L_{rs}(t))\,, \tag{10}$$

with $f(t)$ any function dependent on t. The combination of operators is defined as

$$D_{i_1 i_2 i_3 \ldots i_n} = D_{i_1 i_2} D_{i_2 i_3} \cdots D_{i_{n-1} i_n}\,. \tag{11}$$

One should perform a cyclic permutation of the S/C indices to obtain channels Y and Z. The S/C positions are required to compute the light travel time (LTT) of the armlength $L_{rs}(t)$ between them. For this reason, we use the orbits computed for each S/C. The LTT will affect the delay operators Eq. (10) as well as the projection of the strain onto the links Eq. (4).

To perform data analysis, optimal combinations of the channels X, Y and Z can be found to obtain quasi orthogonal channels. They are defined as [47–51, 54]

$$A = \frac{1}{\sqrt{2}}(Z - X), \tag{12a}$$

$$E = \frac{1}{\sqrt{6}}(X - 2Y + Z), \tag{12b}$$

$$T = \frac{1}{\sqrt{3}}(X + Y + Z). \tag{12c}$$

In this analysis, we work only with channels A and E, as T is almost blind to GWs [54].

II. METHODOLOGY

We aim to test for the presence of deviations from GR in the ringdown of MBHBs with a LISA prototype pipeline. To this end, we developed a code [55] capable of generating ringdown waveforms with the LISA response. Anticipating the detailed description that will be given in a separate paper [55], we describe the main features of the code in the following section.

A. Data

The analysis procedure consists of generating a toy model describing the ringdown phase of a MBHB as the sum of damped oscillations with the response of LISA. The sum of damped oscillations in the ringdown of MBHB is given by Eq. (1), with

$$h_{lmn}(t) = \frac{M_f}{D_l} A_{lmn}(\Xi, t) e^{i(\phi_{lmn}(\Xi,t) - \tilde{\omega}'_{lmn} t)}. \tag{13}$$

The complex frequency with a tilde includes an allowed fractional deviation from GR in the real and the imaginary part, as first introduced by [16],

$$\omega'_{lmn} = \omega^{\rm GR}_{lmn}(M_f, a_f)(1 + \delta\omega_{lmn}), \tag{14a}$$

$$\tau'_{lmn} = \tau^{\rm GR}_{lmn}(M_f, a_f)(1 + \delta\tau_{lmn}). \tag{14b}$$

Then,

$$\tilde{\omega}'_{lmn} = \omega'_{lmn} + i/\tau'_{lmn}. \tag{15}$$

The GR index indicates the values obtained within the GR framework. There are different ways to compute complex frequencies; we recommend [56] for a review on this topic. Here, we make use of the `qnm` package [57] which is based on a spectral eigenvalue approach [58].

Furthermore, Ξ in the amplitude and phase stands for the intrinsic redshifted parameters of the progenitors $\Xi = (m_1, m_2, \chi_1, \chi_2)$, and D_l is the luminosity distance of the source. The spheroidal harmonics in Eq. (1) can be expanded as

$${}_sS_{lmn} = {}_sY_{lm} + \sum_{l \neq l'} \frac{\langle sl'm|\, \mathfrak{h}_1\, |slm\rangle}{l(l+1) - l'(l'+1)} + \cdots , \tag{16}$$

where we drop the dependence on $(a_f\tilde{\omega}_{lmn}; \theta, \varphi)$ for clarity, and where

$$\mathfrak{h}_1 = a_f^2 \omega^2 \cos^2\theta - 2a_f\omega s \cos\theta, \tag{17}$$

and

$$\langle sl'm|\mathfrak{h}_1|slm\rangle = \int_\Omega d\Omega\, {}_sY^*_{l'm}\mathfrak{h}_1\, {}_sY_{lm}. \tag{18}$$

The functions ${}_sY_{lm}$ are the spin-weighted spherical harmonics and $d\Omega$ is the solid angle. It is easy to see in Eqs. (16) and (17) that one can recover the solution for the non-rotating (Schwarzchild) BH in the spherical harmonic basis when $a_f \to 0$.

Mode mixing arises naturally from the choice of representation in perturbation theory in terms of spheroidal harmonics, as opposed to the spherical harmonics which is the most natural representation in numerical relativity (NR). Various authors [59, 60] computed the values of the spheroidal-spherical mixing coefficients, given by

$$\sigma_{l'm'lmn}(a_f) = \delta_{m'm} \int_\Omega {}_{-2}Y^*_{l'm'}(\theta)\, {}_{-2}S_{lmn}(a_f\tilde{\omega}_{lmn}; \theta) d\Omega. \tag{19}$$

Since $\delta_{m'm}$ is the Kronecker delta parameter, we can drop the prime in the first m. Thus, one can find these coefficients in the literature, written without the first m at

TABLE I. Parameters for MBHB injection

Parameter	Value	Parameter	Value
$m_1(M_\odot)$	9384087	$m_2(M_\odot)$	3259880
χ_1	0.555	χ_2	-0.525
ι (rad)	$\pi/3$	ϕ (rad)	$\pi/4$
β (rad)	$\pi/2$	λ (rad)	$\pi/3$
D_l(Mpc)	50000	q	2.878
$M_f(M_\odot)$	1.2175649 $\times 10^7$	a_f	0.821
$\delta\omega_{220}$	0.0	$\delta\tau_{220}$	0.0
$\delta\omega_{330}$	0.01	$\delta\tau_{330}$	0.05
$\delta\omega_{440}$	0.03	$\delta\tau_{440}$	0.1
SNR	587		

all $\sigma_{l'lmn}$ or even written as $\mu_{ml'ln}$. With this representation, the strain has the form

$$h_+(t) - ih_\times(t) = \sum_{l'}\sum_{lmn} h_{lmn}(t)\sigma_{l'mlmn}(a_f)\,{}_{-2}Y_{l'm}. \tag{20}$$

In our case, the amplitudes and phases used in Eq. (13) belong to fittings made by London et al. [61, 62], where the mode mixing is already accounted for. Thus we consider amplitudes with (Eq. [illegible])

$$A_{l'mn} = A_{lmn}\sigma_{l'mlmn}. \tag{21}$$

Therefore, in order to consider the following three QNMs, namely $[(2,2,0),(3,3,0),(4,4,0)]$, we include $[(2,2,2,2,0),(3,2,2,2,0),(3,3,3,3,0),(3,3,3,3,0),$ $(4,4,4,4,0)]$, see Eq. (21). Indeed, the resulting signal is a sum of decaying waves with amplitudes and phases for $lmn = [(2,2,0),(3,3,0),(4,4,0)]$.

We inject a fractional deviation of QNMs equal to $\delta\omega_{lmn} = [0.0, 0.01, 0.03]$ and $\delta\tau_{lmn} = [0.0, 0.05, 0.01]$ in the same QNM order, i.e. $lmn = [(2,2,0),(3,3,0),(4,4,0)]$. Of course, more QNMs could and should be added, but as a proof of concept, we decided to include only these three, leaving more complex searches for future work. We consider input data including a GW signal with and without noise. The sampling rate is set to 1 second as a compromise between the planned sampling rate of 0.25 s, the typical duration of the ringdown for a heavy source (about 7000 s for a mass of $10^7\ M_\odot$) and the number of data points 8192. The parameters used for the source injection are listed in Table I. Note that we use ι as the inclination angle instead of θ. We also write the ringdown SNR as well as the final parameters for the remnant BH obtained with Eqs. (3.6) and (3.8) from [63].

B. Templates

We consider two approaches where the recovery template takes different forms: the *agnostic approach* and the *deviation approach*. In the *agnostic approach*, we assume that the ringdown waveform is described by

$$h_+ - ih_\times = \sum_k A_k e^{i(\phi_k - t\tilde{\omega}_k)}. \tag{22}$$

Here, complex frequencies, amplitudes, and phases can take any value. Note also that any dependence on the spheroidal harmonic is absorbed in the amplitude and the phase. In this way, no *mode mixing* is specified. For example, in this approach, it would not be possible to know how much of the $(2,2,0)$ QNM contribution comes from the spherical harmonic $(2,2)$ or the $(3,2)$. It differs from Eq. (1) as no assumption is made on the value of the complex frequency nor the spherical contribution to any QNM. Despite the fixed number of modes k, we can call this approach "agnostic".

In the *deviation approach*, we assume the framework of GR as baseline but allow for a small "deviation" in the complex frequencies

$$h_+ - ih_\times = \sum_{lmn} A_{lmn} e^{-t/\tau'_{lmn} + i(\phi_{lmn} - t\omega'_{lmn})}, \tag{23}$$

where ω'_{lmn} and τ'_{lmn} are the deviated frequency and damping time from Eqs. (14). In this case, one recovers GR when the deviations are zero. We impose which QNMs are present and look for each pair of deviations. We then compare the results from both approaches and discuss the information one can extract from them.

In our toy model, the injection and the recovery template have the same starting time. In this way, no error is introduced in the waveform due to the uncertainty of the ringdown starting time. Consequently, we do not try to evaluate any systematic uncertainties coming from the definition of the starting time of the ringdown, which is itself ill-defined [64–66]. However, when dealing with real data, where one does not know the appropriate starting point, several starting times in the vicinity of the luminosity peak should be considered (see for example [30, 31, 35]). We also fix the sky localization to the true value. Thus, no error from this parameter is introduced in the waveform either. We leave both issues to be explored in the future.

C. Bayesian analysis

The posterior distribution of the signal parameters $\boldsymbol{\theta}$ given the observed data d, in a Bayesian approach, is expressed as

$$p(\boldsymbol{\theta}|d, M) = \frac{p(d|\boldsymbol{\theta}, M)\,p(\boldsymbol{\theta}|M)}{p(d|M)}, \tag{24}$$

where $\boldsymbol{\theta}$ is the vector of the source physical parameters, M is the model or any other feature considered. In the numerator, we have the likelihood $\mathcal{L}(\theta) = p(d|\boldsymbol{\theta}, M)$ and the prior of the parameters $\pi(\theta) = p(\boldsymbol{\theta}|M)$. In the numerator, $\mathcal{Z} = p(d|M)$ is the evidence, which is computed as the integral of the likelihood over the whole parameter's hyper-volume. For a noise with a covariance matrix $\mathbf{C}$, the likelihood [illegible] form

$$\mathcal{L} = \frac{1}{\sqrt{\det(2\pi\mathbf{C})}} e^{-\frac{1}{2}(d-h(\boldsymbol{\theta})|\mathbf{C}^{-1}|d-h(\boldsymbol{\theta}))}, \tag{25}$$

whose [illegible]

$$\ln\mathcal{L} = -\frac{1}{2}(d-h(\boldsymbol{\theta})|d-h(\boldsymbol{\theta})) + \text{const}, \tag{26}$$

if the noise covariance is fixed. We drop the dependence on the model M and we use the definition of the inner product i[illegible]n

$$(a|b) = \sum_{i,j=0}^{N-1} a_i(\boldsymbol{\theta})\mathbf{C}_{ij}^{-1} b_j(\boldsymbol{\theta}), \tag{27}$$

where N determines the time step $N * \Delta t = T$ of the total t[illegible] the log-likelihood as

$$\ln\mathcal{L} = (d|h(\boldsymbol{\theta})) - \frac{1}{2}(h(\boldsymbol{\theta})|h(\boldsymbol{\theta})) - \frac{1}{2}(d|d). \tag{28}$$

The full log-likelihood is a sum over the log-likelihoods of the uncorrelated instrumental channels A and E (as we ignore the [illegible]). Then, we can write

$$\ln\mathcal{L} = \sum_{I=A,E} \ln\mathcal{L}_I. \tag{29}$$

To obtain the covariance matrix, we use the same method as in [67] with an analytical power spectral density (PSD). Namely, one can create the covariance matrix as a symmetric Toeplitz matrix, assuming stationarity, such that

$$\mathbf{C}_{ij} = \rho(|i-j|), \tag{30}$$

where $\rho(k)$, $k = |i-j|$, is the autocovariance function (ACF) that can be estimated from noise-only data in TD with a length longer than N or as the inverse Fourier transform of the PSD. In our case, we use the latter option, generating the ACF from the LISA Science Requirements D[illegible]

$$\rho(k) = \frac{1}{2T}\sum_{j=0}^{N-1} S(|f_j|)e^{2\pi ijk/N}. \tag{31}$$

Working with matrices usually requires long computational time and special care must be taken because of their numerical instability. To reduce the computational time, one can use different methods such as the Cholesky decomposition [69] or the Levinson recursion [70, 71] among others. To compute fast inner products, we use the **bayesdawn** package [72]. More accurately, we make use of the implemented preconditioned conjugate gradient (PCG) [73] and the Jain method [74] to avoid numerical errors and to fast compute the values of the vectors

$$\overline{a}_j(\boldsymbol{\theta}) = a_i(\boldsymbol{\theta})\mathbf{C}_{ij}^{-1}. \tag{32}$$

Then, the inner product of Eq. (27) becomes a much faster product [illegible]

$$(a|b) = \sum_{j=0}^{N-1} \overline{a}_j(\boldsymbol{\theta}) b_j(\boldsymbol{\theta}). \tag{33}$$

IV. RESULTS

As mentioned in Sec. III B, we consider two analysis approaches. For each approach, we perform two runs: with and without noise. In the following, we discuss the results with noisy data obtained with the **dynesty** [75] sampler.

A. Agnostic approach

In the *agnostic* approach the parameters are $\boldsymbol{\theta} = \{A_k, \phi_k, \omega_k, \tau_k\}$ with $k = 1, 2, 3$ accounting for the three QNMs $[(2,2,0), (3,3,0), (4,4,0)]$. To avoid any degeneracy between the modes, we impose the condition of hyper-triangulation in the frequency. This condition restricts the second frequency to be larger than the first one, and the third to be larger than the second. Then, the uniform prior of each frequency decreases relative to the previous one, like an inverted triangle in the prior's volume. The amplitudes have a logarithmic uniform prior in $[-23, -16]$, as well as the frequency in $[-5, 0]$ and the damping time in $[0, 6]$. The phase is allowed to take any value in the range $[0, 2\pi]$.

In Fig. 1, we present the posterior distribution of the injection without noise in red, with noise in blue, and the injected values with black lines. Remember that the values of the deviations injected in the waveform have been introduced in Table I. We show 12 parameters, 4 for each QNM. In general, the Gaussian distributions converge to the true values, with some minor fluctuations in the noisy case, as expected. In the figure we have already labeled the name of the QNMs "k" since we know them from the injection. However, we will not know which modes are present in the future LISA data analysis. Therefore, one must first find the QNM corresponding to each label $k = lmn$.

One could identify the QNMs by comparing the values of the complex frequencies (ω_k, τ_k) with pairs of (ω_{lmn}, τ_{lmn}) corresponding to an assumed mass and spin obtained from an IMR analysis carried out beforehand. We present the idea of this approach in Fig. 2. The scatter points correspond to the values of the posterior distribution for $k = 1$ in purple, $k = 2$ in pink, and $k = 3$ in green. The colored crosses correspond to the values

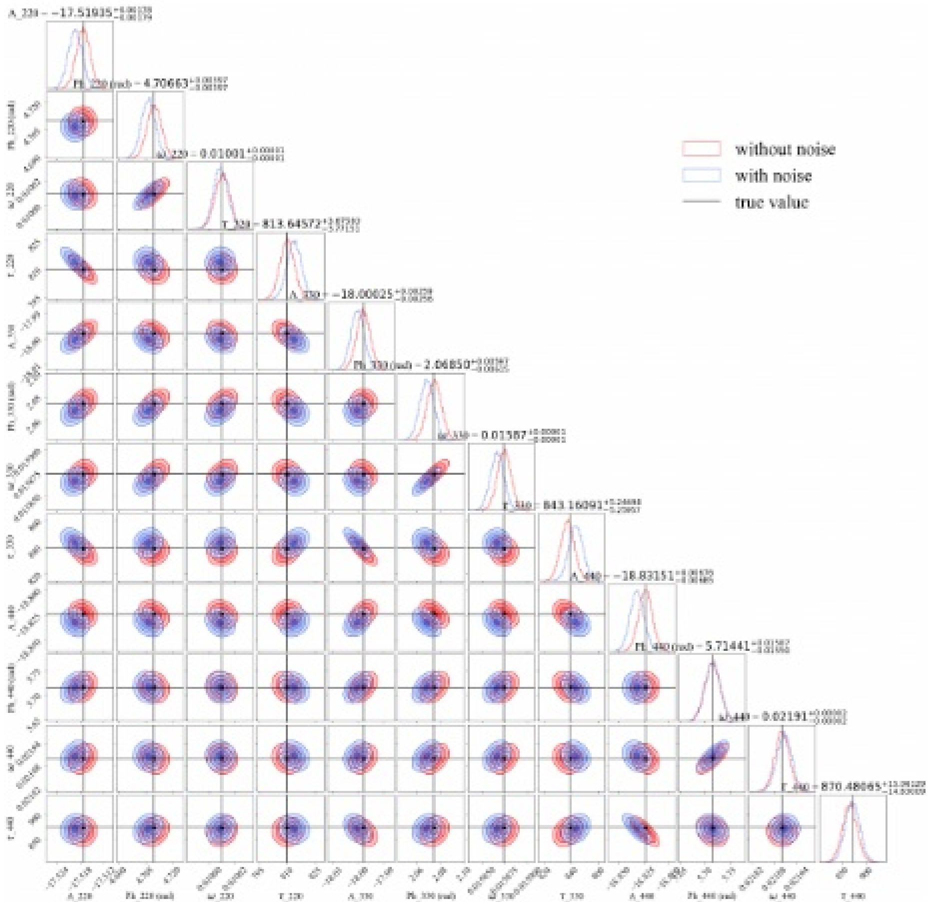

FIG. 1: Posterior distribution for the *agnostic* case with 4 dimensions per mode $\{A_k, \phi_k, \omega_k, \tau_k\}$. Posterior distribution without noise injection in red, with noise injection in blue and injected values marked with black lines. Overall the distributions agree with the true values, with some fluctuations in the noisy case as expected.

of (ω, τ) easily identified with the QNMs labels written nearby. By looking at this figure, we can already state that there might be a deviation from GR, as there is only one mode that we can confidently identify with the posterior distributions, that is $k : 1 = (2, 2, 0)$. The other two clusters of points could be assigned to their nearest QNM, namely $k : 2 = (3, 3, 0)$ and $k : 3 = (4, 4, 0)$. At this stage, one could make one of the two following hypotheses:

(i) The IMR estimation is trustworthy and the final mass and spin are taken to be the true values. In this case, the dominant mode could exhibit deviations from GR as well as all the other harmonics.

(ii) The IMR estimation on mass and spin itself can have systematic errors. Therefore, the analysis should be done by relying only on QNMs. We can identify a QNM that does not present a deviation of GR and assume the inferred mass and spin from that QNM as the true value.

One possible way to check for consistency between QNMs is to trace back the mass and spin of the remnant BH, using the fitting formulas from [23]:

$$M\omega_{lmn} = f_1 + f_2(1-j)^{f_3}, \tag{34a}$$

$$\omega_{lmn}\tau_{lmn}/2 = q_1 + q_2(1-j)^{q_3}, \tag{34b}$$

with $f_1, f_2, f_3, q_1, q_2, q_3$ fitting parameters from Tables

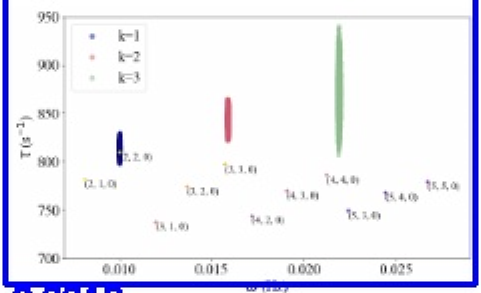

FIG. 2: Posterior distribution of the pairs of complex frequencies in the spectrum map. Each mode 'k' is associated to one colour, purple, pink or green. The spectrum of the true BH is represented with coloured crosses with their QNM label nearby.

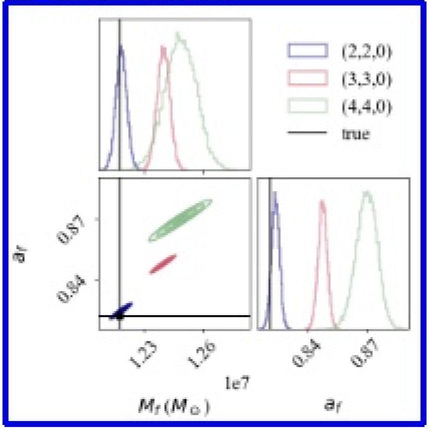

FIG. 3: Posterior distribution for the mass and spin computed with Eq.(34) for each pair of $(\omega_{lmn}, \tau_{lmn})$. Note the agreement of $(2, 2, 0)$ with the true value while the other two modes diverge, showing a deviation from GR in those modes.

(VIII, IX, X) in [23]. With any pair of (ω, τ) one can compute first the value of the spin and then the value of the mass.

If we take samples within each mode's posterior distribution in Fig. 2 and use Eqs. (34) to compute the corresponding masses and the spins, we obtain the distributions in Fig. 3. We perceived already from Fig. 2 that the posteriors of the mass and spin obtained from different QNMs would not overlap completely. Here we can confirm it by observing three different mean values for the spin without any overlap and three distributions for the mass with overlap between values computed from $(3, 3, 0)$ in pink and $(4, 4, 0)$ in green. Notably, the true value in black does not fit perfectly with the mean value of the $(2, 2, 0)$ in purple. This is due to small fluctuations in the (ω, τ) mean value, which can be seen in Fig 1, and the fact that Eqs. (34) come from a fitting and thus, intrinsic errors of the order of $\sim 1 - 3\%$ [23] are expected in the mass and the spin.

To better understand the differences in the posteriors, one could alternatively follow the approach adopted in [26]. That is, using Eqs. (34) to compute the value of the mass for a given spin and comparing the values obtained from different QNMs. Note, that this approach does not propagate errors from the spin fitting into the mass, as it remains fixed. This representation can be seen in Fig 4, where the true value is marked with a golden or a black star, and the shadow lines correspond to the 90% credible levels. The standard deviation for the mass is related to the standard deviations of ω and τ. As a result of the precision on the frequencies posteriors, the uncertainty bands derived from ω_{lmn} are relatively narrow. The mass and spin obtained from the $(2, 2, 0)$ mode are consistent with the injected value, while the others exhibit deviations from it.

[illegible] masses and spins as references

We can now discuss the first hypothesis (i) stated above. Imagine we want to quantify the deviation in each mode's frequency to put some constraints on an alternative theory. In that case, we have to compare the posterior distributions of frequency and damping time with the QNM values for a BH with the IMR estimated final mass and spin. To simplify, we assume that the parameters estimated from the IMR analysis equal the exact injected values. Results can be seen in Fig. 5, where we subtract the true complex frequency value from each mode. In this figure, we can see that each posterior agrees with the injected value within 2σ. The dashed blue lines mark the quantiles (0.16, 0.84), i.e., the 1σ distribution.

However, using reference values for the mass and spin is somewhat inconsistent with the agnostic philosophy. Keep in mind that, the mean values estimated from an IMR analysis could present a bias. Moreover, using the whole parameter posterior distribution instead of mean values would better allow for the propagation of uncertainties.

[illegible] on QNM characterization

Without a posterior distribution from an IMR waveform inference, we now adopt the second of the two above hypotheses and use the mass and spin obtained from the dominant mode as reference values. While we already showed above that the dominant mode agrees within a 90% credible confidence with the injected parameters, there is a risk in assuming that the $(2, 2, 0)$ mode does

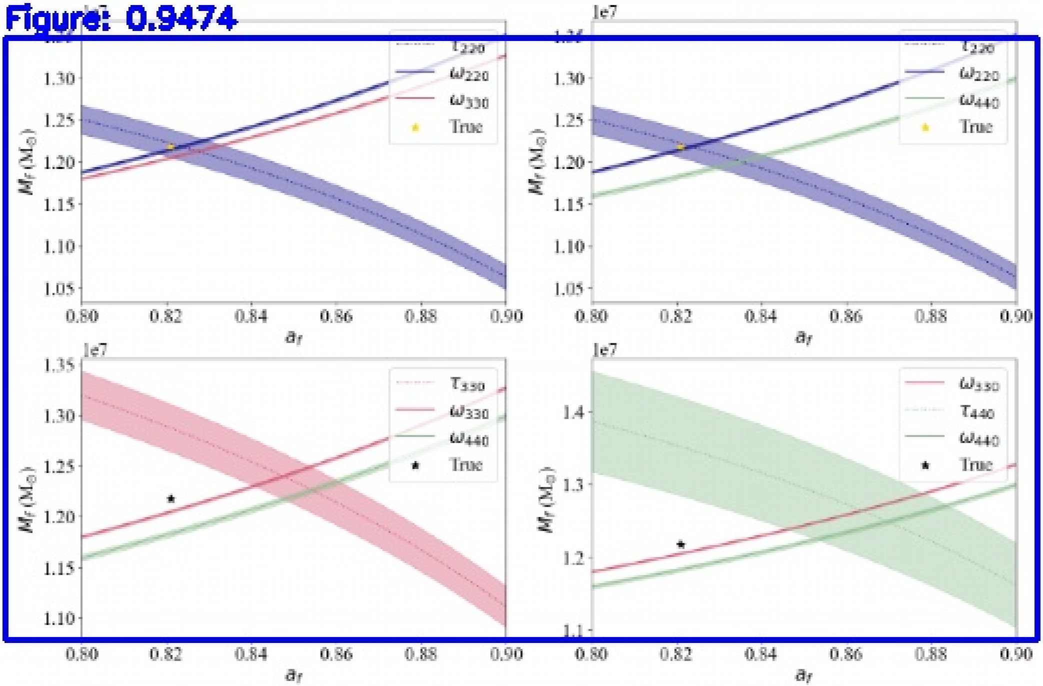

FIG. 4: Computed mass for spins in the range [0.8-0.9] with Eq.34 with a 99% confidence level, from the estimated mean values of $(\hat{M}_{lmn}, \hat{a}_{lmn})$.

not deviate from GR. Correspondingly, deviations in the dominant mode might also appear.

Now, to quantify the deviations in this framework, we should translate the differences in mass and spin into deviations in ω and τ in terms of $\delta\omega, \delta\tau$, see Eqs. (14), (15). To this end, we assumed that the posterior distribution obtained from the $(2,2,0)$ mode is the "true" description of the remnant BH in GR. We can then compute the QNM spectrum with the derived mass and spin from that mode. This computation is shown in Fig 6, where we observe the posterior of the three complex frequencies $\tilde{\omega}_{lmn}$ computed with the mass and spin derived from the dominant mode $\{\hat{M}_{f220}, \hat{a}_{f220}\}$. The GR values are marked with colored crosses on top of the distributions. As stated, deviations might appear in the $(2,2,0)$ mode. Thus, comparing the mass and spin estimated from this BH spectroscopy with those inferred from the full IMR waveforms would be informative.

Given the distributions without deviations, one can measure the one-dimensional deviation for each parameter. To this aim, we need to compare the complex frequency (lmn) posteriors with the values obtained from the mass and spin corresponding to the $(2,2,0)$ mode $(\hat{M}_{f220}, \hat{a}_{f220})$ for each mode. This is analogous as comparing Fig. 3 with Fig. 6. The results are shown in the top row of Fig. 7, where we find the distribution of GR complex frequencies computed with the mass and spin derived from the $(2,2,0)$ mode for the $(3,3,0)$ mode in pink, and in green for the $(4,4,0)$ mode. We can easily distinguish them from the non-GR values obtained from the posteriors in blue. A simple equation to quantify this tension is commonly used [76, 77]:

$$N_\sigma = \frac{|\mu_A - \mu_B|}{\sqrt{\sigma_A^2 + \sigma_B^2}}, \tag{35}$$

where A and B are two different models, μ is the estimated mean value and σ is the standard deviation. This equation gives the number of standard deviations between two posterior distributions in one dimension. This simple definition can be used as a means to estimate uncertainties in the following. For the injected values of Table I, the computed standard deviation from GR values is shown in Table II. Should this be observed, we would have detected a deviation from GR in ω_{330} with more than 10 standard deviations relative to the $(2,2,0)$ mode. It is also important to note that even though we

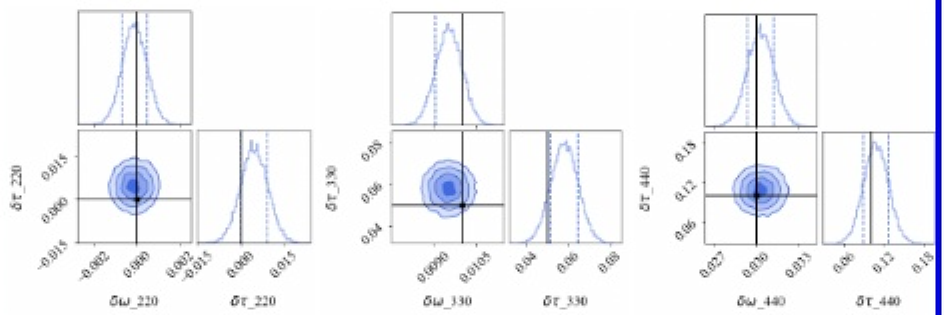

(a) Fractional deviation obtained in ω_{220} and τ_{220} (b) Fractional deviation obtained in ω_{330} and τ_{330} (c) Fractional deviation obtained in ω_{440} and τ_{440}

FIG. 5: Posterior distribution of the fractional deviations in the complex frequency obtained from the posterior distribution of mass and spin, compared with the GR QNMs with true values of M_f, a_f, for the modes $k = lmn$.

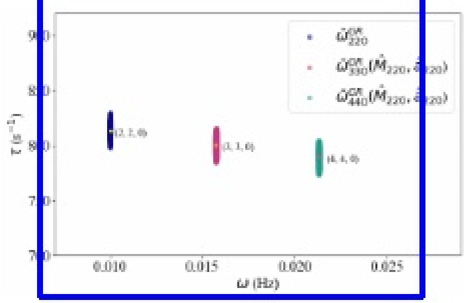

FIG. 6: Posterior distribution of each mode, generated from the posterior distribution of mass and spin derived from the (2,2,0) mode, compared with true spectrum.

distinguished a deviation from GR with high precision, the injected value does not correspond to the recovered value, thus revealing a bias.

To summarize, with the hypothesis (*ii*) this kind of analysis would allow one to differentiate GR from another theory. However, when attempting to constrain an alternative theory, the recovered values of the deviations might lead to misinterpretations. This can be seen in the bottom row of Fig. 7, where the injected value (in black) does not appear consistent with the posterior distribution. For these two bottom figures, we use the blue posterior distributions from the top row and subtract the mean value of the pink and green posteriors respectively. Indeed, the estimated value shown in Fig. 7c, is inconsistent with $\delta\omega_{330} = 0.01$. This is because we used the GR value derived from the mass and spin inferred from the $(2, 2, 0)$ mode characterization, for which we assumed no deviation. Even if the mass and spin computed from the $(2, 2, 0)$ mode agree with the true values, the assumption of no deviation in this mode might have strong implications, as any fluctuation on the $(2, 2, 0)$ mode will translate into fluctuations in the estimated mass and spin and therefore in the subsequent characterization of the $(3, 3, 0)$ and $(4, 4, 0)$ modes. Certainly, the computation of the QNMs highly depends on the mass and spin, thus small variations of those intrinsic parameters translate to larger variations on the complex frequency parameter space.

TABLE II: Computed uncertainty from GR for the injected parameters in the agnostic case.

	$N_{\sigma GR}(3,3,0)$	$N_{\sigma GR}(4,4,0)$
$\delta\omega$	10.31	28.46
$\delta\tau$	7.97	5.62

One can avoid this type of discrepancy by using the posterior distribution of the mass and spin inferred from the full IMR instead of the posterior inferred from the $(2, 2, 0)$ mode. Again, this implies that the IMR analysis should provide unbiased values. In the present analysis, the mass and spin from the $(2, 2, 0)$ mode were consistent within 2σ with the injected value.

B. Deviation approach

In the following, we discuss the results of the second approach, the *deviation* template. For this search, we have to define beforehand which QNMs appear in the waveform. We also assume that the dominant mode does not have deviations from GR. Imposing this condition allows us to break the degeneracy between the mode's fractional deviations from GR and the BH mass and spin. Alternatively, one could fix the mass and the spin, but allow the whole QNM spectrum to present deviations.

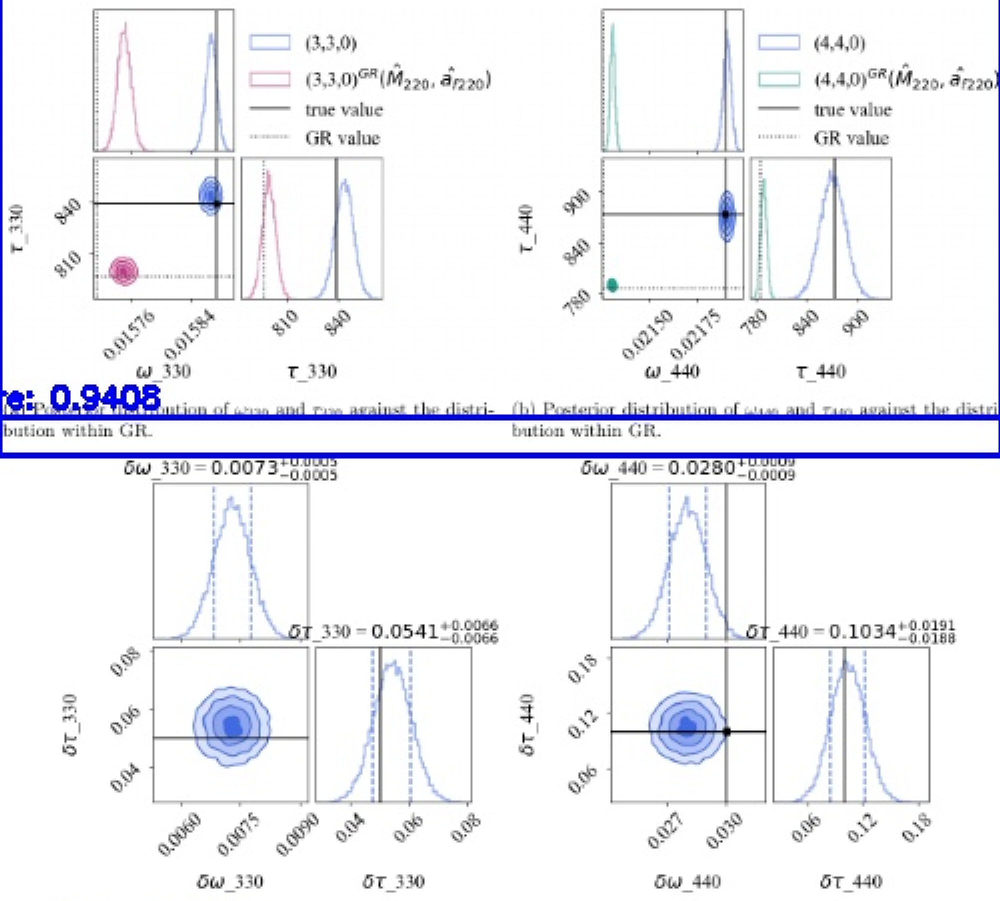

(a) Posterior distribution of ω_{330} and τ_{330} against the distribution within GR.

(b) Posterior distribution of ω_{440} and τ_{440} against the distribution within GR.

(c) Fractional deviation from GR for $\tilde{\omega}_{330}$.

(d) Fractional deviation from GR for $\tilde{\omega}_{440}$.

FIG. 7: Evidence of deviations in the frequency and damping time computed with the estimated final mass and spin. The top row shows the posterior distribution of the complex frequency for each mode in blue, against the computed posterior distribution in the GR framework for the parameters derived from the (2,2,0) modes in pink and green. In the bottom row, we subtract the mean value of the estimated GR QNM from the obtained posterior distribution. By doing so, the fractional deviation becomes evident. The damping time agrees with the injected value (black lines) for both modes, while the frequency presents a bias due to the high sensitivity to the remnant parameters estimated from the (2,2,0) mode.

The parameters in this second approach are $\boldsymbol{\theta} = \{M_f, a_f, A_{220}, \phi_{220}, A_k, \phi_k, \delta\omega_k, \delta\tau_k\}$ with k=$[(3,3,0),(4,4,0)]$. The mass and spin have a uniform prior within a range of 10% around the injected value, which gives the intervals $[0.9, 1.1] \times M_f$ and $[0.9, 1.1] \times a_f$, respectively. The phase has a uniform prior in the range $[0, 2\pi]$, while the amplitudes have a logarithmic uniform prior in $[-23, -16]$. Lastly, the deviations have a uniform prior in the range $\delta\omega, \delta\tau = [-0.2, 0.2]$. This range arises naturally from the chosen QNMs, as the relative difference between two QNMs is bigger than 0.2:

$$\frac{|\omega_{220} - \omega_{330}|}{\omega_{220}} > 0.2. \tag{36}$$

For QNMs with closer spectrum such as $(2,2,0)$ and

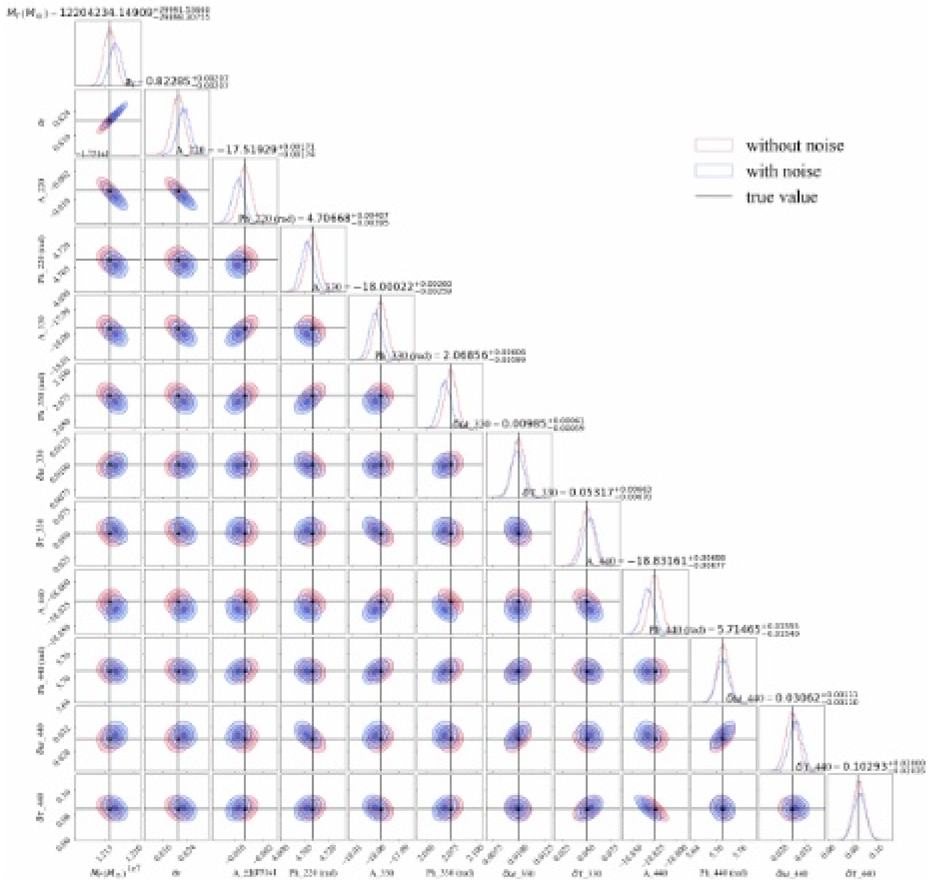

FIG. 8: Posterior distribution for the *deviation* case. Results without noise injection in red, with noise injection in blue, and injected value with black lines. Overall the distributions agree with the true values, with some fluctuations as the noisy case is expected.

$(2,2,1)$, there is a possible switching on the labels producing a degeneracy between those two modes and exhibiting a bimodal posterior distribution. For this reason, we do not include the QNM $(2,2,1)$ in the analysis, even though its presence might have been detected in GW150914 [30] albeit the small significance (see the discussion in [30–35]). We leave this particular case to be studied in the future.

In Fig. 8 we show the posterior distribution with and without noise injection in blue and red respectively. Injected values are marked with black lines. We observe the consistency between both results with the true values.

Note that in this approach, the analysis is straightforward. The fractional deviations in the spectrum directly result from the posteriors since the deviations found in each QNM account for the estimated mass and spin by construction. In Fig. 9 we zoom in on the deviations of the $[(3,3,0),(4,4,0)]$ modes and recover the injected values with high accuracy and precision. The uncertainty on the deviations from GR parameters $\delta\omega$ and $\delta\tau$ with this template are listed in Table III. Note that under the same hypothesis (ii) as in previous analysis, i.e. no deviation in the $(2,2,0)$ is observed, it is possible to derive constraints on an alternative theory, since the injected values are within the posterior distributions. A caution message is imperative here. The template considered, by construction, does not allow for deviations in the dominant mode. The effect of a fractional deviation in the

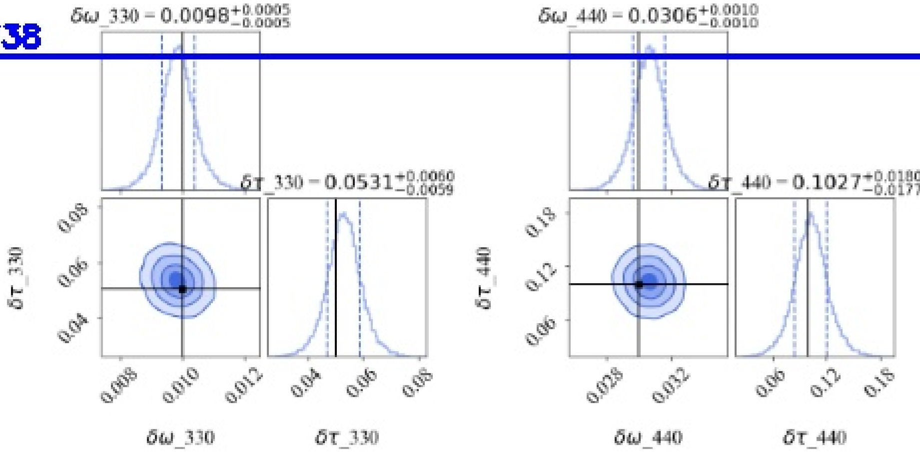

(a) Fractional deviations in (3,3,0) (b) Fractional deviations in (4,4,0)

FIG. 9: Posterior distribution of fractional deviations in modes (3,3,0) and (4,4,0) directly from the sampler. Dashed lines denote the 1σ error and black lines the injected value. We obtain agreeing results with high precision.

(2, 2, 0) mode, when not considered in the search template needs further investigation. Nevertheless, in order to constrain an alternative theory the model-independent template might not be enough and specific templates for beyond-GR theories are required.

Given that the value of the standard deviation for each parameter is inversely proportional to the SNR, there is a way to estimate the SNR needed to observe a specific deviation from GR with a given uncertainty in terms of standard deviation. We expand on this idea in Sec. V.

C. Discussion

In the perspective of testing the no-hair theorem and possible deviations from GR with the LISA instrument, we explore the extent to which we can extract the largest amount of information through two different analyses in terms of two generic templates. One possible approach is to compare the posterior distribution of fractional deviations in frequency and damping times $\delta\omega_k, \delta\tau_k$ from different templates.

We compare both methods in Fig. 10, where the posterior distributions of deviations for the *agnostic* approach are shown in green and the results for the *deviations* approach are in orange. We denote the injected values by black lines. Under the same assumption of no deviation from GR in the (2, 2, 0) mode, the deviation approach gives more accurate results, making it possible to constrain alternative theories to GR. In the agnostic result, the premise that no deviation from GR affects the (2, 2, 0) mode has strong implications. If one relaxes this constraint and assumes that the IMR estimation is accurate enough to fix the mass and the spin values, then a deviation in the dominant mode can be considered and the deviations of higher harmonics would be consistent with the injected values, as seen in Fig. 5. However, this result will strongly depend on the estimated mass and spin from the full IMR analysis, whose values can be biased if features like higher harmonics, eccentricity, or precession, to name only a few, are not considered.

TABLE III: Computed deviation uncertainty from GR for the injected parameters in the *deviation* approach.

	$N_{\sigma\mathrm{GR}}(3,3,0)$	$N_{\sigma\mathrm{GR}}(4,4,0)$
$\delta\omega$	16.34	27.81
$\delta\tau$	7.98	5.06

V. TEST OF GR VERSUS SNR

In what follows, we discuss the SNR needed to claim a deviation from GR with different parameters. To this aim, we will use the *deviation* template, which provides the best consistency under the assumptions taken. We compute the standard deviation

$$\sigma_{\theta_i} = \sqrt{\Gamma^{-1}_{ii}}, \tag{37}$$

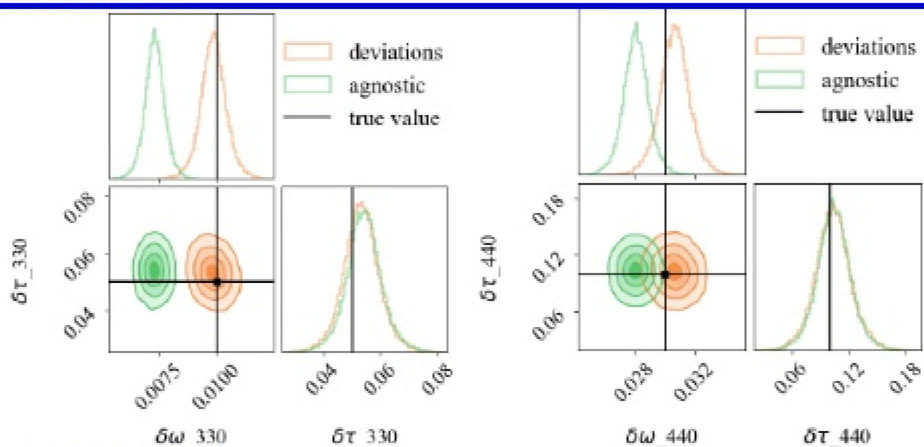

(a) Fractional deviation for (3,3,0) mode with both methods

(b) Fractional deviation for (4,4,0) mode with both methods

FIG. 10: Comparison of the posterior distribution of the fractional deviations for modes (3,3,0) and (4,4,0) for the two different methods. Posterior distributions obtained for the *deviation* approach are shown in orange and green for the *agnostic* approach. The black lines intersections mark the injected values.

where Γ_{ij} is the Fisher matrix computed with the inner product defined in Eq. [illegible]

$$\Gamma_{ij} = (a(\boldsymbol{\theta}_i)|b(\boldsymbol{\theta}_i)). \tag{38}$$

The results are presented in Table IV, showing the consistency between the error obtained from the Bayesian analysis with the Fisher forecast. Even if the Fisher matrix underestimates the uncertainty for $\delta\tau_{440}$, possibly due to the noise injection, we can still extract information from the other parameters.

From Eq. (37) we see how the uncertainty varies as the inverse of the SNR, so naturally the standard deviation in the different parameters decreases as the SNR increases. Consequently, for a given source, it is related to the total mass and the luminosity distance. We can therefore estimate the mass and the redshift needed to claim a deviation from GR with 5σ. Of course, the number of sigmas N_σ is constrained by the value of the fractional deviation itself, as shown in Eq. (35).

TABLE IV: Uncertainty computed with the Fisher matrix (second column) and obtained with the sampler (third column)

	$\sigma_{\rm FM}$	$\sigma_{\rm sampler}$
$\delta\omega_{330}$	0.587×10^{-3}	0.602×10^{-3}
$\delta\tau_{330}$	6.252×10^{-3}	6.648×10^{-3}
$\delta\omega_{440}$	1.047×10^{-3}	1.101×10^{-3}
$\delta\tau_{440}$	11.978×10^{-3}	20.28×10^{-3}

We show in Fig. 11 the uncertainty for the parameters with possible deviations from the GR values using the *deviation* template, such as $(\delta\omega_{330}, \delta\tau_{330}, \delta\omega_{440}, \delta\tau_{440})$. Several assumptions have been made from the beginning of the study, therefore the result we present does not provide a general detection forecast. Nevertheless, this analysis provides a qualitative understanding of LISA's ability to observe deviations from GR in the ringdown phase of a MBHB coalescence. The uncertainty on the fractional deviations is represented as a function of the source total mass and the redshift which are the dominant contributors to the SNR. We let all other source parameters fixed to the same values listed in Table I. Consequently, the estimates shown in Fig. 11 are source-dependent, i.e., valid for the particular BH we chose as a case study. Another choice of BH parameters would change this result. Different inclinations, spins, and mass ratios would inevitably change the relative amplitude between QNMs and thus the uncertainty in each mode's complex frequency.

The color code on the right-hand side of Fig. 11 indicates the value of the uncertainty on the fractional QNM frequencies, obtained with the Fisher matrix for the considered example source. For instance, areas where $\sigma \leq 0.005$ show that LISA should be able to detect deviations from GR in $\delta\omega_{330}$ at the level of 5 standard deviations or more if the departure from GR is of the order of 0.025 taking $\delta^{GR} = 5\sigma$, for sources between 10^6 to 10^7 $M_\odot$ through the whole universe, i.e. for any possible redshift. Considering more precision favorable situations, a

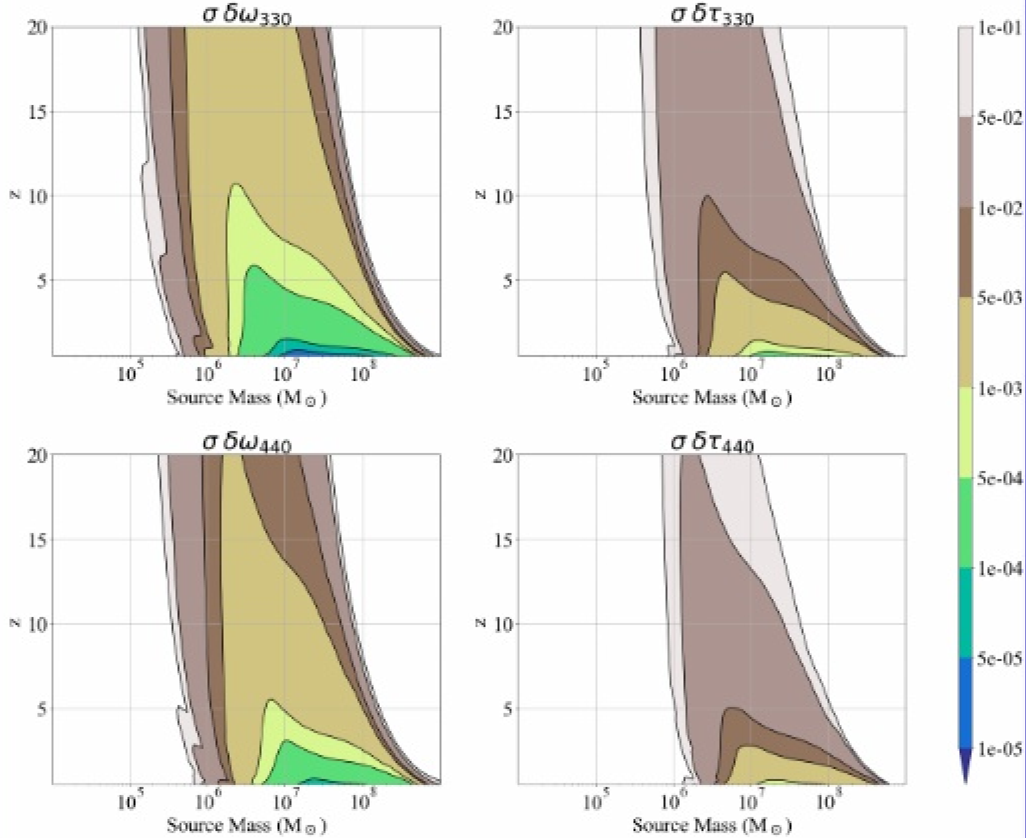

FIG. 11: Uncertainty for fractional deviations from GR in ω and τ in modes (3,3,0) and (4,4,0) with respect to the source total mass and the redshift. These values are obtained for the fixed parameters listed in Table I.

deviation from GR of 5×10^{-4} would be distinguishable for sources below redshift 1 and total mass of the order of $10^7\,M_\odot$. At first glance, one could conclude that the most severe limits will come from the deviations or lack of them in the frequencies $\delta\omega_{lmn}$ because of the high sensitivity of LISA to frequency variations. The expected population of MBHB for heavy seeds encloses sources in the range $[10^4 - 10^7]\,M_\odot$ up to redshift 10 approximately. This range is extended to lower-mass sources in the case of light seeds [43, 78, 79]. Hence, even if LISA cannot observe some of these golden sources, the expectation to test the no-hair theorem and GR looks very promising for "nearby" sources ranging in the mass interval $[10^6 - 10^7]\,M_\odot$.

VI. CONCLUSIONS

In this study, we use two approaches to explore the no-hair theorem with LISA: the *agnostic* approach where no assumption on the source parameters is made except on the number of observable QNMs; and the *deviations* approach, where fractional deviations of specific QNMs are estimated.

The advantage of the *agnostic* approach is that it does not require any hypothesis on the events, except for the number of QNMs (which could also be inferred by performing a Bayesian model comparison not demonstrated here). We estimate the frequency and damping time for each QNM. By comparing the mass and spin derived from the complex frequencies we identify different values for each QNM, resulting in inconsistency between QNMs in the GR framework. We also quantify these deviations as fractional deviations from GR, which entails a delicate interpretation of the results depending on the assumptions made. Indeed, the non-GR-deviation hypothesis in the dominant mode is too restrictive to correctly identify the injected deviation for each QNM, despite being consistent within 2σ with the true values. However, this kind of discrepancy can be circumvented by contrasting the results with the posterior distributions obtained from the IMR analysis, presuming that physical effects like eccentricity or others are included to avoid biased parameters. Hence this procedure requires an unbiased IMR analysis to compare results to.

The *deviation* approach shows better results for the fractional deviation values. However, prior assumptions are required to recover the injected values. Particularly, we assume a fixed number of observable QNMs and further constraints in the priors volume. Using the fact that no significant deviation in the first mode is observed, we do not need to rely on an IMR analysis since the intrinsic BH parameters are estimated. Including the mass and spin in the parameter estimation enables us to absorb small variations that correspond to relatively large errors in the QNMs. Thus, the hypothesis of non-deviation in the dominant mode allows us to find the injected QNM deviations confidently. If one allows for deviations in the dominant mode, extra care or further constraints in the priors are necessary due to the degeneracy between M_f, a_f and $\delta\omega_{220}, \delta\tau_{220}$. Such an analysis is left for the future.

Consequently, combining both methods could improve the characterization of possible deviations from GR. Thus, one optimized method would be to perform an *agnostic* search to determine a descriptive set of QNMs and a raw estimation of the mass and spin to be compared to the IMR parameters. Once this is done, specific deviations for each QNM could be targeted, taking special care in the priors probability definition for each mode, as mode degeneracies and label switching may arise.

Finally, we also evaluate the impact of redshift and total mass on the observable deviations from GR in the BH's spectrum with the *deviation* template. From this analysis, we can estimate that in the best-case scenario, i.e., with "golden" sources, the strong regime of GR could be tested up to 5×10^{-3}%. However, these sources do not dominate the estimated population of black holes in the heavy or light seeds models. Nevertheless, the prospects of testing GR in the ringdown signal from sources with masses $[10^6 - 10^7]\ M_\odot$ at redshift ≤ 5 are very promising, with a detectable fractional deviation of $\delta\omega_{330} \leq 5 \times 10^{-2}$% in the $(3, 3, 0)$ mode's frequency.

ACKNOWLEDGMENTS

We wish to thank Sylvain Marsat for his valuable insights. This work was supported by CNES, focused on LISA Mission. We gratefully acknowledge support from the CNRS/IN2P3 Computing Center (Lyon - France) for providing computing and data-processing resources needed for this work. CP acknowledges financial support from CNES Grant No. 51/20082 and CEA Grant No. 2022-035.

[1] B. P. Abbot *et al.*, Ligo: the laser interferometer gravitational-wave observatory, Reports on Progress in Physics **72**, 076901 (2009).
[2] J. Aasi *et al.*, Advanced ligo, Classical and Quantum Gravity **32**, 074001 (2015).
[3] B. P. Abbott *et al.* (LIGO Scientific Collaboration and Virgo Collaboration), Observation of gravitational waves from a binary black hole merger, Phys. Rev. Lett. **116**, 061102 (2016).
[4] B. P. Abbott *et al.* (The LIGO Scientific Collaboration and the Virgo Collaboration), Tests of general relativity with the binary black hole signals from the ligo-virgo catalog gwtc-1, Phys. Rev. D **100**, 104036 (2019).
[5] B. P. Abbott *et al.* (LIGO Scientific and Virgo Collaborations), Tests of general relativity with gw150914, Phys. Rev. Lett. **116**, 221101 (2016).
[6] R. Abbott *et al.* (LIGO Scientific Collaboration and Virgo Collaboration), Tests of general relativity with binary black holes from the second ligo-virgo gravitational-wave transient catalog, Phys. Rev. D **103**, 122002 (2021).
[7] R. Abbott *et al.* (The LIGO Scientific Collaboration and the Virgo Collaboration), Tests of general relativity with gwtc-3 (2021), arXiv:2112.06861 [gr-qc].
[8] B. Carter, Axisymmetric black hole has only two degrees of freedom, Phys. Rev. Lett. **26**, 331 (1971).
[9] K. G. Arun *et al.*, New horizons for fundamental physics with lisa, Living Reviews in Relativity , 4 (2022).
[10] S. A. Teukolsky, Perturbations of a Rotating Black Hole. I. Fundamental Equations for Gravitational, Electromagnetic, and Neutrino-Field Perturbations, The Astrophysical Journal **185**, 635 (1973).
[11] W. H. Press and S. A. Teukolsky, Perturbations of a Rotating Black Hole. II. Dynamical Stability of the Kerr Metric, The Astrophysical Journal **185**, 649 (1973).
[12] C. V. Vishveshwara, Stability of the schwarzschild metric, Phys. Rev. D **1**, 2870 (1970).
[13] S. L. Detweiler, Resonant oscillations of a rapidly rotating black hole, Proc. Roy. Soc. Lond. A **352**, 381 (1977).
[14] S. Chandrasekhar and S. Detweiler, The quasi-normal modes of the schwarzschild black hole, Proceedings of the Royal Society of London. A. Mathematical and Physical Sciences **344**, 441 (1975), https://royalsocietypublishing.org/doi/pdf/10.1098/rspa.1975.0112.
[15] S. Detweiler, Black holes and gravitational waves. III - The resonant frequencies of rotating holes, Astrophys. J. **239**, 292 (1980).
[16] I. Kamaretsos, M. Hannam, S. Husa, and B. S. Sathyaprakash, Black-hole hair loss: Learning about bi-

nary progenitors from ringdown signals, Physical Review D **85**, 10.1103/physrevd.85.024018 (2012).

[17] I. Kamaretsos, M. Hannam, and B. S. Sathyaprakash, Is black-hole ringdown a memory of its progenitor?, Physical Review Letters **109**, 10.1103/physrevlett.109.141102 (2012).

[18] K. D. Kokkotas and B. G. Schmidt, Quasi-normal modes of stars and black holes, Living Reviews in Relativity **2**, 10.12942/lrr-1999-2 (1999).

[19] H.-P. Nollert, Quasinormal modes: the characteristic 'sound' of black holes and neutron stars, Classical and Quantum Gravity **16** (1999).

[20] F. Echeverria, Gravitational-wave measurements of the mass and angular momentum of a black hole, Phys. Rev. D **40**, 3194 (1989).

[21] L. S. Finn, Detection, measurement, and gravitational radiation, Physical Review D **46**, 5236–5249 (1992).

[22] O. Dreyer, B. Kelly, B. Krishnan, L. S. Finn, D. Garrison, and R. Lopez-Aleman, Black-hole spectroscopy: testing general relativity through gravitational-wave observations, Classical and Quantum Gravity **21**, 787 (2004).

[23] E. Berti, V. Cardoso, and C. M. Will, Gravitational-wave spectroscopy of massive black holes with the space interferometer LISA, Physical Review D **73**, 10.1103/physrevd.73.064030 (2006).

[24] C. Molina, P. Pani, V. Cardoso, and L. Gualtieri, Gravitational signature of schwarzschild black holes in dynamical chern-simons gravity, Physical Review D **81**, 10.1103/physrevd.81.124021 (2010).

[25] O. J. Tattersall and P. G. Ferreira, Quasinormal modes of black holes in horndeski gravity, Phys. Rev. D **97**, 104047 (2018).

[26] S. Gossan, J. Veitch, and B. S. Sathyaprakash, Bayesian model selection for testing the no-hair theorem with black hole ringdowns, Physical Review D **85**, 10.1103/physrevd.85.124056 (2012).

[27] T. Accadia *et al.*, Virgo: a laser interferometer to detect gravitational waves, Journal of Instrumentation **7** (3), 3012.

[28] Y. Aso, Y. Michimura, K. Somiya, M. Ando, O. Miyakawa, T. Sekiguchi, D. Tatsumi, and H. Yamamoto (The KAGRA Collaboration), Interferometer design of the kagra gravitational wave detector, Phys. Rev. D **88**, 043007 (2013).

[29] V. Gennari, G. Carullo, and W. D. Pozzo, Searching for ringdown higher modes with a numerical relativity-informed post-merger model (2023), arXiv:2312.12515 [gr-qc].

[30] M. Isi, M. Giesler, W. M. Farr, M. A. Scheel, and S. A. Teukolsky, Testing the no-hair theorem with GW150914, Physical Review Letters **123**, 10.1103/physrevlett.123.111102 (2019).

[31] M. Giesler, M. Isi, M. A. Scheel, and S. A. Teukolsky, Black hole ringdown: The importance of overtones, Physical Review X **9**, 10.1103/physrevx.9.041060 (2019).

[32] R. Cotesta, G. Carullo, E. Berti, and V. Cardoso, Analysis of ringdown overtones in gw150914, Phys. Rev. Lett. **129**, 111102 (2022).

[33] M. Isi and W. M. Farr, Revisiting the ringdown of gw150914 (2022), arXiv:2202.02941 [gr-qc].

[34] M. Isi and W. Farr, Comment on "analysis of ringdown overtones in gw150914", Physical Review Letters **131**, 10.1103/physrevlett.131.169001 (2023).

[35] G. Carullo, R. Cotesta, E. Berti, and V. Cardoso, Carullo et al. replay, Physical Review Letters **131**, 10.1103/physrevlett.131.169002 (2023).

[36] E. steering committee *et al.*, Einstein telescope: Science case, design study and feasibility report. et-0028a-20 (2020).

[37] P. Amaro-Seoane *et al.*, Laser Interferometer Space Antenna, arXiv e-prints , arXiv:1702.00786 (2017), arXiv:1702.00786 [astro-ph.IM].

[38] A. Ghosh, R. Brito, and A. Buonanno, Constraints on quasinormal-mode frequencies with ligo-virgo binary–black-hole observations, Phys. Rev. D **103**, 124041 (2021).

[39] E. Maggio, H. O. Silva, A. Buonanno, and A. Ghosh, Tests of general relativity in the nonlinear regime: a parametrized plunge-merger-ringdown gravitational waveform model (2023), arXiv:2212.09655 [gr-qc].

[40] J. L. Blázquez-Salcedo, C. F. Macedo, V. Cardoso, V. Ferrari, L. Gualtieri, F. S. Khoo, J. Kunz, and P. Pani, Perturbed black holes in einstein-dilaton-gauss-bonnet gravity: Stability, ringdown, and gravitational-wave emission, Physical Review D **94**, 10.1103/physrevd.94.104024 (2016).

[41] L. Pierini and L. Gualtieri, Quasinormal modes of rotating black holes in einstein-dilaton gauss-bonnet gravity: The first order in rotation, Physical Review D **103**, 10.1103/physrevd.103.124017 (2021).

[42] P. A. Cano, K. Fransen, T. Hertog, and S. Maenaut, Quasinormal modes of rotating black holes in higher-derivative gravity (2023), arXiv:2307.07431 [gr-qc].

[43] L. S. S. Team, Lisa redbook (2024), in preparation.

[44] C. Pitte, Q. Baghi, S. Marsat, M. Besançon, and A. Petiteau, Detectability of higher harmonics with lisa, Phys. Rev. D **108**, 044053 (2023).

[45] A. Toubiana, L. Pompili, A. Buonanno, J. R. Gair, and M. L. Katz, Measuring source properties and quasi-normal-mode frequencies of heavy massive black-hole binaries with lisa (2024), arXiv:2307.15086 [gr-qc].

[46] R. Brito, A. Buonanno, and V. Raymond, Black-hole spectroscopy by making full use of gravitational-wave modeling, Physical Review D **98**, 10.1103/physrevd.98.084038 (2018).

[47] M. Tinto and J. W. Armstrong, Cancellation of laser noise in an unequal-arm interferometer detector of gravitational radiation, Phys. Rev. D **59**, 102003 (1999).

[48] M. Tinto, F. B. Estabrook, and J. W. Armstrong, Time delay interferometry with moving spacecraft arrays, Physical Review D **69**, 10.1103/physrevd.69.082001 (2004).

[49] J. W. Armstrong, F. B. Estabrook, and M. Tinto, Time-delay interferometry for space-based gravitational wave searches, The Astrophysical Journal **527**, 814 (1999).

[50] M. Tinto, F. B. Estabrook, and J. W. Armstrong, Time-delay interferometry for lisa, Phys. Rev. D **65**, 082003 (2002).

[51] F. B. Estabrook, M. Tinto, and J. W. Armstrong, Time-delay analysis of lisa gravitational wave data: Elimination of spacecraft motion effects, Phys. Rev. D **62**, 042002 (2000).

[52] M. Vallisneri, Geometric time delay interferometry, Phys. Rev. D **72**, 042003 (2005), [Erratum: Phys.Rev.D 76, 109903 (2007)], arXiv:gr-qc/0504145.

[53] J.-B. Bayle, O. Hartwig, and M. Staab, Adapting time-delay interferometry for LISA data in frequency, Physical Review D **104**, 10.1103/physrevd.104.023006 (2021).

[54] T. A. Prince, M. Tinto, S. L. Larson, and J. W. Armstrong, Lisa optimal sensitivity, Phys. Rev. D **66**, 122002 (2002).

[55] C. Pitte, J.-B. Bayle, and Q. Baghi, Lisaring, in preparation.

[56] E. Berti, V. Cardoso, and A. O. Starinets, Quasinormal modes of black holes and black branes, Classical and Quantum Gravity **26**, 163001 (2009).

[57] L. C. Stein, qnm: A Python package for calculating Kerr quasinormal modes, separation constants, and spherical-spheroidal mixing coefficients, J. Open Source Softw. **4**, 1683 (2019), arXiv:1908.10377 [gr-qc].

[58] G. B. Cook and M. Zalutskiy, Gravitational perturbations of the kerr geometry: High-accuracy study, Physical Review D **90**, 10.1103/physrevd.90.124021 (2014).

[59] L. London, S. Khan, E. Fauchon-Jones, C. García, M. Hannam, S. Husa, X. Jiménez-Forteza, C. Kalaghatgi, F. Ohme, and F. Pannarale, First higher-multipole model of gravitational waves from spinning and coalescing black-hole binaries, Physical Review Letters **120**, 10.1103/physrevlett.120.161102 (2018).

[60] E. Berti and A. Klein, Mixing of spherical and spheroidal modes in perturbed kerr black holes, Physical Review D **90**, 10.1103/physrevd.90.064012 (2014).

[61] L. London, Modeling ringdown. ii. aligned-spin binary black holes, implications for data analysis and fundamental theory, Physical Review D **102**, 10.1103/physrevd.102.084052 (2020).

[62] L. London, D. Shoemaker, and J. Healy, Modeling ringdown: Beyond the fundamental quasinormal modes, Physical Review D **90**, 10.1103/physrevd.90.124032 (2014).

[63] S. Husa, S. Khan, M. Hannam, M. Pürrer, F. Ohme, X. J. Forteza, and A. Bohé, Frequency-domain gravitational waves from nonprecessing black-hole binaries. i. new numerical waveforms and anatomy of the signal, Phys. Rev. D **93**, 044006 (2016).

[64] S. Bhagwat, M. Okounkova, S. W. Ballmer, D. A. Brown, M. Giesler, M. A. Scheel, and S. A. Teukolsky, On choosing the start time of binary black hole ringdowns, Physical Review D **97**, 10.1103/physrevd.97.104065 (2018).

[65] S. Bhagwat, X. J. Forteza, P. Pani, and V. Ferrari, Ringdown overtones, black hole spectroscopy, and no-hair theorem tests, Physical Review D **101**, 10.1103/physrevd.101.044033 (2020).

[66] V. Baibhav, M. H.-Y. Cheung, E. Berti, V. Cardoso, G. Carullo, R. Cotesta, W. D. Pozzo, and F. Duque, Agnostic black hole spectroscopy: quasinormal mode content of numerical relativity waveforms and limits of validity of linear perturbation theory (2023), arXiv:2302.03050 [gr-qc].

[67] M. Isi and W. M. Farr, Analyzing black-hole ringdowns (2021).

[68] LISA Science Study Team, *LISA Science Requirements Document*, Requirement Document ESA-L3-EST-SCI-RS-001-i1.0 (ESA, 2018) `https://www.cosmos.esa.int/web/lisa/lisa-documents/`.

[69] C. Benoit, Note sur une méthode de résolution des équations normales provenant de l'application de la méthode des moindres carrés a un système d'équations linéaires en nombre inférieur a celui des inconnues. — application de la méthode a la résolution d'un système defini d'équations linéaires, Bulletin géodésique **2**, 67 (1924).

[70] N. Levinson, The wiener (root mean square) error criterion in filter design and prediction, Journal of Mathematics and Physics **25**, 261 (1946), https://onlinelibrary.wiley.com/doi/pdf/10.1002/sapm1946251261.

[71] J. Durbin, The fitting of time-series models, Revue de l'Institut International de Statistique / Review of the International Statistical Institute **28**, 233 (1960).

[72] Q. Baghi, Bayesdawn (2020).

[73] E. Kaasschieter, Preconditioned conjugate gradients for solving singular systems, Journal of Computational and Applied Mathematics **24**, 265 (1988).

[74] A. Jain, Fast inversion of banded toeplitz matrices by circular decompositions, IEEE Transactions on Acoustics, Speech, and Signal Processing **26**, 121 (1978).

[75] J. S. Speagle, DYNESTY: a dynamic nested sampling package for estimating Bayesian posteriors and evidences, Monthly Notices of the Royal Astronomical Society **493**, 3132 (2020), arXiv:1904.02180 [astro-ph.IM].

[76] M. Leizerovich, S. J. Landau, and C. G. Scóccola, Tensions in cosmology: a discussion of statistical tools to determine inconsistencies (2023), arXiv:2312.08542 [astro-ph.CO].

[77] P. Lemos *et al.*, Assessing tension metrics with dark energy survey and planck data, Monthly Notices of the Royal Astronomical Society **505**, 6179–6194 (2021).

[78] E. Barausse, I. Dvorkin, M. Tremmel, M. Volonteri, and M. Bonetti, Massive black hole merger rates: The effect of kiloparsec separation wandering and supernova feedback, The Astrophysical Journal **904**, 16 (2020).

[79] E. Barausse and A. Lapi, Massive black-hole mergers, in *Handbook of Gravitational Wave Astronomy* (Springer Singapore, 2021) p. 1–33.